1   Revision 2   Word Count: 6306

Isotopic responses of Mg to two types of dissolution-reprecipitation processes for the growth of the double-carbonate mineral norsethite

CHUAN LIU[1], KAI WANG[1], WEIQIANG LI[1,*]

[1] State Key Laboratory for Mineral Deposits Research, School of Earth Sciences and Engineering, Nanjing University, Nanjing, Jiangsu 210093, PR China

ABSTRACT

An important mechanism of carbonate mineral growth is dissolution-reprecipitation, including the transformation of amorphous precursor to crystalline carbonates, and coarsening (ripening) of fine carbonate crystals. However, the mechanistic details of cation exchange associated with carbonate mineral growth via a dissolution-reprecipitation process are still not well understood. In this study, we used Mg isotopes to probe the exchange of Mg between aqueous solutions and norsethite [$BaMg(CO_3)_2$] by systematic synthesis experiments. Norsethite is a model double carbonate, with a general formula of $AB(CO_3)_2$, where A and B stand for two different divalent ions. Formation of norsethite comprised of three stages, including 1) precipitation of barium-magnesium amorphous carbonate, 2) transformation of

23   Ba-Mg amorphous carbonate to nano-crystalline norsethite by fast

24   dissolution-reprecipitation, and (3) coarsening (ripening) of nano-norsethite by slow

25   dissolution-reprecipitation. Magnesium isotopes displayed distinct fractionation

26   behaviors in each of the three stages. The Mg isotope fractionation factors

27   ($\Delta^{26}Mg_{solid-aq}$) associated with precipitation of Ba-Mg amorphous carbonate were

28   slightly negative and temperature-dependent, from -0.83‰ at 30°C to -0.53‰ at 70°C.

29   During the transformation of Ba-Mg amorphous carbonate to nano-crystalline

30   norsethite, isotopically light Mg isotopes were further enriched in the solid phase,

31   with apparent $\Delta^{26}Mg_{solid-aq}$ decreasing to -2.12‰ at 30°C and -1.56‰ at 70°C. In the

32   ripening stage, norsethite became isotopically heavier, with $\Delta^{26}Mg_{solid-aq}$ increasing up

33   to -1.95‰ at 30°C and -1.17‰ at 70°C. The experimental results show that

34   non-equilibrium isotope fractionation occurred during the transformation of

35   amorphous carbonate to nano-crystalline norsethite (i.e., fast

36   dissolution-reprecipitation), by contrast, the subsequent ripening of the norsethite led

37   to the evolution towards isotopic equilibrium of the system by slower exchange with a

38   longer reaction time (i.e., slow dissolution-reprecipitation). Notably, the results of first

39   principle calculation indicate the equilibrium isotope fractionation was approached,

40   but not attained, even after 276 days of recrystallization at temperatures below 70°C.

41   This study identified two different types of dissolution-reprecipitation process during

42   the carbonate mineral growth and highlights the importance of understanding

43   formation mechanism and post-depositional history of carbonate for interpreting the

44   isotopic data in carbonate minerals.

45

46   Key words:

47

48   Norsethite, amorphous carbonate; dissolution-reprecipitation; transformation;

49   recrystallization; Mg isotope

50

INTRODUCTION

52

53   Carbonates comprise a major component of the ancient sedimentary records (e.g.,

54   Morse and Mackenzie, 1990) and they are of great importance in geological record, as

55   they document a variety of geological, environmental, and biological processes.

56   Carbonate is a ubiquitous material and plays an essential role in human society, such

57   as construction, agriculture, and mechanical engineering (e.g., Børja and Nilsen, 2009;

58   De Muynck et al., 2008; Gu et al., 2008; Jin and Yue, 2008; Wang et al., 2021). For a

59   better interpretation of carbonate geochemical records and industrial applications, it is

60   important to understand the mechanism that controls carbonate nucleation and

61   growth.

62

63   Carbonates could grow via different mechanisms. Numerous studies have been

64   conducted to study the formation of carbonate minerals, focusing on the classic

65   crystal growth mechanism of ion-by-ion attachment (e.g., Davis et al., 2000; De Yoreo

66   et al., 2013; Hong et al., 2016; Nielsen et al., 2016; Teng et al., 2000). However, the

67 formation of carbonate minerals could proceed via an alternative, yet fundamental

68 pathway, which is the transformation of amorphous carbonate precursor (e.g., Giuffre

69 et al., 2015; Liu and Li, 2020; Loste et al., 2003; Mavromatis et al., 2017b;

70 Rodriguez-Blanco et al., 2017), a kind of metastable material with the microscopic

71 structure that lacks long-range order. Carbonate formation via the pathway of

72 transformation of amorphous carbonate is particularly important for biomineralization.

73 Phenomena of amorphous carbonate transformation have been reported in many

74 biologically precipitated carbonates (Gower, 2008 and references therein), such as

75 foraminifera (Jacob et al., 2017; Mor Khalifa et al., 2018), coral skeletons (Mass et al.,

76 2017; Sun et al., 2020; Von Euw et al., 2017), sea urchin spicule (Politi et al., 2008;

77 Raz et al., 2003) and mollusk shells (Baronnet et al., 2008; Weiss et al., 2002).

78 Transformation of amorphous carbonate could take place via a coupled

79 dissolution-reprecipitation mechanism (e.g., Giuffre et al., 2015; Liu and Li, 2020;

80 Purgstaller et al., 2016). Furthermore, once the carbonate minerals form, the

81 recrystallization, which is one of the most fundamental changes for carbonates during

82 the diagenesis process (Fantle et al., 2020), takes place by continuous

83 dissolution-reprecipitation mechanism and will not stop until the minerals are

84 completely isolated from surrounding fluids. Therefore, dissolution-reprecipitation is

85 one of the key mechanisms governing the formation and growth of carbonate minerals.

86 However, the nature and kinetics of atom/ion exchange during the

87 dissolution-reprecipitation of carbonates are still not completely understood (Burdige

88 et al., 2010; Gorski and Fantle, 2017; Hu and Burdige, 2007; Reeves and Rothman,

89   2013; Zamanian et al., 2016). Yet dissolution-reprecipitation of carbonates exerts

90   strong controls on the elemental and isotopic signatures of carbonates, which are vital

91   information for a variety of applications, such as reconstructing the evolution

92   seawater chemistry (pH, redox conditions, and chemical composition) (e.g., Bialik et

93   al., 2018; Higgins and Schrag, 2012; Rae et al., 2011; Ries, 2004; Rollion-Bard et al.,

94   2011; Zhang et al., 2018) and paleo-climate (e.g., Bice et al., 2006; Lachniet, 2009;

95   McDermott, 2004; Mitsuguchi et al., 1996; Wang et al., 2001), as well as tracing the

96   diagenesis process (Banner, 1995; Derry et al., 1992; Swart, 2015 and references

97   therein), etc.

98

99   Magnesium is a common component in carbonates and its isotopes have been applied

100   to paleoenvironmental and paleographic studies (Crockford et al., 2020; Fantle and

101   Higgins, 2014; Gothmann et al., 2017; Higgins and Schrag, 2012; Li et al., 2015; Liu

102   et al., 2018; Pogge von Strandmann et al., 2014). Moreover, isotopes can provide

103   unique information for mineral dissolution, precipitation, as well as ion exchange

104   between minerals and fluids (e.g., Chanda et al., 2019; Frierdich et al., 2019; Gorski

105   and Fantle, 2017; Liu and Li, 2020; Zhu et al., 2020). Therefore, Mg isotopes in

106   carbonate   hold   a   promise   for   elucidating   some   key   aspects   of   the

107   dissolution-reprecipitation process. In this study, we conducted systematic low

108   temperature (30 to 80°C) synthesis experiments of norsethite [$BaMg(CO_3)_2$]. We

109   documented the mineralogical characteristics of solid products and Mg isotope

110   evolution of both mineral and co-existing solution. Norsethite is similar in lattice

5

111 structure to dolomite and has been extensively studied to reveal the formation

112 pathway of dolomite (Effenberger et al., 2014; Lindner and Jordan, 2018; Pimentel

113 and Pina, 2014; Pimentel and Pina, 2016; Pimentel et al., 2021; Zhang et al., 2021).

114 The experimental results, supplemented by *ab initio* calculations of equilibrium Mg

115 isotope fractionation, reveal links between different carbonate mineral growth

116 processes and Mg isotope fractionation behaviors and provide new insights about the

117 fidelity of the Mg isotope ratios as a geochemical tool in carbonate records.

118

119 **EXPERIMENTAL METHODS**

120

121 **Chemicals**

122

123 For the experiments, gravimetrically weighted reagent grade salts of $MgCl_2 \cdot 6H_2O$,

124 $BaCl_2 \cdot 2H_2O$, Na_2CO_3, and deionized water (18.2 $M\Omega \cdot cm^{-1}$), were used to prepare the

125 reactant solutions. The reactant solutions include "solution A1" (2M $MgCl_2$),

126 "solution A2" (2M $MgCl_2$ prepared from a different batch of $MgCl_2 \cdot 6H_2O$ salt, which

127 has different Mg isotope composition compared to "solution A1"), "solution B" (1M

128 $BaCl_2$), and "solution C" (1M Na_2CO_3). All the experiments and subsequent analyses

129 were conducted at the State Key Laboratory for Mineral Deposits Research, Nanjing

130 University, China.

131

132 **Synthesis experiment**

6

133

134   The experiments were systematically performed at temperatures from 30 to 80°C,

135   with a 10°C increment. For the main set of experiments (Set I), 5mL of "solution A1",

136   5mL of "solution B", and 15mL of de-ionized water were mixed in a glass bottle to

137   make a mixed solution that contained 0.4M $MgCl_2$ and 0.2M $BaCl_2$. On the other

138   hand, 10mL of "solution C" and 15mL of de-ionized water were mixed in another

139   glass bottle to make a solution of 0.4M Na_2CO_3. The two bottles were capped and

140   placed in an oven at a preset temperature (30°C, 40°C, 50°C, 60°C, 70°C or 80°C).

141   Twelve hours of thermal equilibration was applied to ensure that the two solutions

142   were at the desired temperature before the Mg-Ba solution was mixed with the

143   Na_2CO_3 solution. Therefore, the initial reaction solution contained 0.2M $MgCl_2$, 0.1M

144    $BaCl_2$ and 0.2M Na_2CO_3. A white cloudy material appeared immediately upon mixing

145   the two solutions. The reaction bottle was then tightly sealed by a rubber stopper and

146   a clamped aluminum cap, and placed on a magnetically stirring hotplate that was set

147   at different temperatures (30°C, 40°C, 50°C, 60°C, 70°C, or 80°C). The temperature

148   stability of the hotplate was monitored by an external temperature sensor that was

149   attached to the bottom of the bottle and the temperature was found to fluctuate

150   periodically. The amplitude of the measured temperature increased with the increase

151   of the set temperature, for example, when the set temperature was 30°C, the

152   corresponding measured temperature ranged from 27.6°C to 32.5°C, and this value

153   was between 72.1°C and 89.1°C when setting the temperature at 80°C (Appendix Fig

154   S1 and Appendix Table S1). An aliquot of 5 mL homogeneous slurry was sampled by

155 pipetting from the reactors after 1 minute, 2 hours, 1 day, 10 days, and 60 days of

156 reaction time after mixing. The slurry was transferred into a centrifuge tube, which

157 was centrifuged at 3000r/min for 5 minutes to separate the solid and liquid phases,

158 and the solid was further washed with de-ionized water and centrifuged three times to

159 remove interstitial fluids. The supernatant was centrifuged at 12000 r/min for 1

160 minute before transfer to a second clean centrifuge tube. This operation was repeated

161 three times to remove all the possible suspending solids from the aqueous solution.

162 The washed solid was separated into different aliquots for elemental, mineralogical,

163 and isotopic analyses.

164

165 Slightly different conditions were used in another set of experiments (Set II). In this

166 experiment set, 2.5mL of "solution A2", 2.5 mL of "solution B" and 20 mL of

167 de-ionized water were mixed in a glass bottle to make a mixed solution that contained

168 0.2M $MgCl_2$ and 0.1M $BaCl_2$ at first, meanwhile, 5mL of "solution C" and 20mL of

169 de-ionized water were mixed in another glass bottle to make a solution of 0.2M

170 Na_2CO_3. Then the Mg-Ba mixing solutions were mixed with Na_2CO_3 solutions. And

171 the bottles were tightly sealed and placed on a magnetically stirring hotplate that was

172 set at different temperatures (30°C, 40°C, 50°C, 60°C, 70°C, or 80°C). Therefore, the

173 initial reaction solution contained 0.1M $MgCl_2$, 0.05M $BaCl_2$ and 0.1M Na_2CO_3.

174 Sampling of 5mL homogeneous slurry was conducted by pipetting from the reactors

175 after 30 days and 276 days of reaction time for this group of experiments. The solid

176 and aqueous phases were separated by the same procedures as used in Set I.

8

177

178 **Mineralogical analyses**

179

180 A small aliquot of the solid product was prepared for scanning electron microscopy

181 (SEM) observations and XRD analysis. The SEM images were taken using a Carl

182 Zeiss Supra 55 Field Emission Scanning Electron Microscope, and Energy-Dispersive

183 X-ray Spectroscopy (EDS) with the SEM was used for semi-quantitative analysis of

184 the chemical compositions of the solids. Additionally, the specific surface area (SSA)

185 of the samples was analyzed by the low-pressure nitrogen adsorption isotherm method

186 (N_2-LPAI) at the MOE Key Laboratory Surficial Geochemistry at Nanjing University

187 (details in Sun et al., 2017). Briefly, the measurements were conducted on a

188 Micrometritics ASAP 2020 HD88 Surface Area and Porosity Analyzer. Before the

189 measurements, the samples, except the amorphous carbonate, were heated in a

190 vacuum oven at 378K for 10 hours for degassing. Then the N_2 adsorption-desorption,

191 with the N_2 pressure from 0.05 to 0.2 atm, isotherm linear plots were obtained at

192 77.3K. The SSA of samples were calculated using Brunauer-Emmet-Teller (BET)

193 method with the isotherm linear plots.

194

195 A Rigaku RAPID II dual-source X-ray diffractometer was used to collect the XRD

196 pattern of the solid product. The instrument was running with a rotating Mo

197 (K_α=0.7093Å) target X-ray source operated at 50 kV and 90 mA. The X-ray

198 diffraction pattern for the products was collected using a two-dimensional image plate

199   with a 10 minute exposure time. Data interpretation was performed using a Rigaku

200   2DP program and Jade 6.5 software.

201

202   **Solution chemistry characterization**

203

204   The pH of solutions was measured using a Mettler Toledo combined electrode, which

205   was calibrated by commercial standard buffers (pH=4.00, 7.00, and 9.21 at 25°C).

206   The precision of each pH measurement was ±0.02 unit. An aliquot of the solution

207   sample in synthesis experiments was taken for alkalinity measurement by titrating

208   with 0.019M HCl and the titration operation was repeated three times; another aliquot

209   was acidified with 2% HNO_3 for Mg^{2+} and Ba^{2+} analysis. Elemental concentration

210   was measured by inductively coupled plasma optical emission spectroscopy (a Skyray

211   ICP3000 type ICP-OES), using gravimetrically prepared multi-element standard

212   solutions. The PHREEQC software was used to calculate the speciation of aqueous

213   solutions, ion activities, and the saturation state of minerals with its *Pitzer* database.

214   The solubility products for hydromagnesite (Gautier et al., 2014) and nesquehonite

215   (Harrison et al., 2019) were included in the database. For all experiments, the pH

216   values were measured at 25°C and recalculated for the experimental temperature in

217   PHREEQC. The saturation index (SI) of norsethite was expressed as:

218     $$SI=\log(\Omega)=\log\left(\frac{(a_{Ba^{2+}})(a_{Mg^{2+}})(a_{CO_3^{2-}})^2}{K_{sp}}\right)$$

219   (1)

220   where *a* represents the activity of an aqueous species, and the solubility product of

221   norsethite is calculated using the function $log_{10}K_{sp}=31.007-7321.122/T-0.0811 \times T$ (T

222   in kelvin, from 313K to 423K, Lindner et al., 2018).

223

224   **Mg isotope analysis**

225

226   Both solid and solution samples were treated with 1mL concentrated nitric acid and

227   evaporated on a hot plate at 95°C. This operation was repeated three times to convert

228   the salts to nitrate form for the column procedure. Then Mg of the solid and aqueous

229   phases was purified following a well-established two-stage column procedure at the

230   State Key Lab for Mineral Deposits Research, Nanjing University (Hu et al., 2017;

231   Liu and Li, 2020). Magnesium isotope analysis was performed using a Thermo

232   Scientific Neptune Plus multi-collector inductively coupled mass spectrometer

233   (MC-ICP-MS) that operated on medium-mass-resolution, wet plasma mode, the

234   details of instrumental parameters are listed in Appendix Table S5. Instrument drift

235   and mass bias were corrected using a standard-sample bracketing routine with an

236   in-house Mg solution (HPS909104) as the bracketing standard (Hu et al., 2017; Li et

237   al., 2015). Magnesium isotope data are reported using the standard delta notation (‰)

238   of $\delta^{26}Mg$ and $\delta^{25}Mg$ for the $^{26}Mg/^{24}Mg$ and $^{25}Mg/^{24}Mg$ ratios relative to the DSM3

239   Mg isotope standard, where

240     $\delta^{x}Mg=\left[\left(\ ^{x}Mg/^{24}Mg_{sample}\right)/\left(\ ^{x}Mg/^{24}Mg_{DSM3}\right)-1\right]\times1000$ (2)

241   and the Mg isotope fractionation factor between two phases A and B is expressed as:

242     $\Delta^{x}Mg_{A-B}=\delta^{x}Mg_{A}-\delta^{x}Mg_{B}\approx10^{3}\ln\alpha_{A-B}^{x/24}$ (3)

11

243   where x=25 or 26.

244

245   The external precision of the Mg isotope measurement was better than ±0.1‰ in

246   δ^{26}Mg. Accuracy of Mg isotope analyses was monitored using pure Mg standards

247   (Cambridge1 and DSM3), natural sample standards (IAPSO standard seawater), and a

248   matrix-matching synthetic standard solution made of $BaCl_2$ and in-house Mg standard

249   HPS932001 (1:1 molar ratio). The natural sample standards and matrix-matching

250   synthetic standard were treated as unknown samples together with samples from

251   experiments by ion-exchange chromatography, to assess the accuracy of the total

252   chemical procedure, and the accuracy was verified to be better than ±0.1‰ in δ^{26}Mg,

253   within the external precision. The measured Mg isotope compositions for both pure

254   Mg standard and standard samples (matrix-matching synthetic standard and seawater)

255   match well with published values (Appendix Table S5).

256

257   **First-principles calculation of the equilibrium mass-dependent isotope**

258   **fractionation**

259

260   To better interpret the experimental data, equilibrium Mg isotope fractionation factors

261   between norsethite and dolomite were calculated using *ab intio* methods. The isotopic

262   fractionation factor between phase A and B is usually defined as $\alpha_{A\text{-}B}=\beta_A/\beta_B$, where β

263   is the reduced partition function ratios or called β-factor. With the harmonic

264   approximation, the β-factor of crystalline solids can be calculated by the following

12

265   formula (Bigeleisen and Mayer, 1947; Urey, 1947):

$$\beta = \left[\prod_{i=1}^{3N_{at}} \prod_{q} \frac{v_{q,i}^*}{v_{qi}} \cdot \frac{e^{-hv_{q,i}^*/(2kT)}}{1-e^{-hv_{q,i}^*/(kT)}} \cdot \frac{1-e^{-hv_{q,i}/(kT)}}{e^{-hv_{q,i}/(2kT)}} \right]^{1/N_q N} \tag{4}$$

266   where $v_{q,i}$ is the vibrational frequency of the ith phonon mode at the wavevector q,

267   which can be derived from the first-principles calculation. N_{at}, N_q, and N represent the

268   number of atoms in a unit cell, phonon wavevectors, and sites of isotopes in the unit

269   cell, respectively. T is the temperature in Kelvin, h is Planck's constant, k is

270   Boltzmann's constant, and the superscript * represents the vibrational frequencies of

271   the system with heavier isotopes.

272

273   First-principles calculations are performed using the VASP package based on the

274   projector-augmented-wave (PAW) method (Kresse and Joubert, 1999). The

275   exchange-correlation energies between electrons are described by the generalized

276   gradient approximations (GGA) of the Perdew-Burke-Ernzerhof scheme for solids

277   (PBEsol) (Perdew et al., 2008). Other functionals, such as PBE (Perdew et al., 1996)

278   and local density approximations (LDA) (Perdew and Zunger, 1981) are also tested.

279   Pseudo-potentials of Ba_sv ($5s^2 5p^6 6s^2$), Ca_sv ($3s^2 3p^6 4s^2$), Mg_pv ($2p^6 3s^2$), C

280   ($3s^2 3p^2$), and O ($2s^2 2p^4$) shipped with VASP are adopted, and plane-wave cutoffs are

281   set to 600 eV. Conventional primitive cells of 30 atoms for norsethite [$Ba_3Mg_3(CO_3)_6$],

282   dolomite [$Ca_3Mg_3 (CO_3)_6$], and magnesite [$Mg_6(CO_3)_6$] are firstly relaxed with

283   variable lattices under the ambient pressure, and further atomic relaxations are

284   performed with fixed cells. The Brillouin zone is sampled by a $3\times3\times1$ k-points grid

285   according to Monkhorst–Pack scheme (Monkhorst and Pack, 1976). The convergence

286   threshold for electronic iteration is 10^{-6} eV, and for structural relaxation, we choose

287   when the residual forces act on atoms are less than 10^{-4} eV/Å. To calculate the phonon

288   frequencies needed in Eq.4, the Hessian matrix is constructed using the finite

289   displacement method implemented in VASP using $2\times2\times1$ supercells, and higher

290   convergence tolerance of 10^{-7} eV/Å is also used to make sure the accuracy of the force

291   calculation. Phonon frequencies are then obtained by using the PHONOPY (Togo and

292   Tanaka, 2015) package, and an $8\times8\times8$ q-point mesh is proven sufficiently to get

293   converged β-factors.

294

295   **RESULTS**

296

297   **Mineralogy**

298

299   The mineralogy and key features of the XRD spectrum of the solid phases are

300   summarized in Appendix Table S2 and Table S3. In experiment Set I, the solid

301   product sampled after 1 minute of the reaction was pure Ba-Mg amorphous carbonate

302   for experiments at 30°C to 70°C. However, for the experiment at 80°C, the solid

303   product sampled after 1 minute of the reaction was a mixture of norsethite and Ba-Mg

304   amorphous carbonate, based on XRD analysis (Fig. 1A). The Ba-Mg amorphous

305   carbonate occurred as spheres with a diameter of 20 to 200 nm irrespective of

306   temperature (Fig. 2A, D and Appendix Fig. S3). The solid product at 80°C consisted

14

307   of Ba-Mg amorphous carbonate spheres and fine norsethite crystals below 50 nm (Fig.

308   2G). After 2 hours of reaction, the amorphous carbonate completely transformed to

309   norsethite in experiments between 40°C to 80°C, whereas the Ba-Mg amorphous

310   carbonate persisted as the solid phase in the experiment at 30°C (Appendix TableS2

311   and Appendix Fig. S2). After 1 day of reaction, the solid phase consisted of only

312   norsethite in all experiments (Appendix Fig. S2). The crystals were anhedral and

313   granular with a size below 50 nm for experiments between 40°C to 70°C (Appendix

314   Fig. S4). In experiments performed at 30°C and 80°C, some larger crystals with more

315   euhedral shapes were observed after 1 day. And after 60 days of reaction, the

316   norsethite crystals became larger and more euhedral with rhombohedra morphology

317   especially at higher temperatures (Fig. 2C, F, I and Appendix Fig. S5). The increase of

318   crystal size was also manifested by the decrease of the SSA of norsethite with a longer

319   reaction time (Fig.1B and Appendix Table. S2).

320

321   XRD analyses confirmed that norsethite was the sole mineral in the solid phase after

322   the disappearance of Ba-Mg amorphous carbonate in all experiments (Appendix Fig.

323   S2), consistent with a previous study conducted under similar conditions (Liu and Li,

324   2020). Notably, the measured d value and the peak sharpness index (Full Width at

325   Half Maximum, or FWHM) of the (104) peak for norsethite decreased with increasing

326   reaction time (Fig. 3A, B, Appendix TableS2). The FWHM of dolomite d(104) peak

327   decreases with increasing crystallinity (Li et al., 2015), and this was consistent with

328   the SEM observations in this study that the crystals became larger and more euhedral

15

329   with increasing time (Fig. 1B). By contrast, the peak intensity ratio I(101)/I(012) and

330   I(015)/I(110), indicators for the cation ordering in the crystal lattice of dolomite-group

331   minerals (e.g., Li et al., 2015; Liu and Li, 2020; Pimentel and Pina, 2014), remained

332   constant irrespective of reaction time (Fig. 3C, D).

333

334   **Solution chemistry**

335

336   The details of solution chemistry are tabulated in Appendix Table S4 for experiment

337   Set I. Solutions sampled after 1 minute of reaction had alkalinity ranging from 33 to

338   38 mM for experiments from 30 to 70°C, however, the alkalinity of solution sampled

339   after 1 minute of reaction at 80°C was much lower (11.5 mM). The alkalinity of

340   solutions decreased to around 10 mM after 2 hours for all experiments, except for the

341   experiment conducted at 30°C, where the alkalinity decreased to around 10 mM after

342   1 day. The decrease in solution alkalinity was temporally related to the disappearance

343   of amorphous carbonate in the solid phase in the experiments. After the complete

344   transformation of Ba-Mg amorphous carbonate to norsethite, the alkalinity of

345   solutions fluctuated between 6 and 12 mM (Appendix Fig. S7A). The pH of the

346   solutions generally increased when Ba-Mg amorphous carbonate transformed to

347   norsethite for all experiments, then pH values decreased continuously with time

348   (Appendix Fig. S7B).

349

350   The Mg concentrations ranged from 80 to 100 mM during the early period of reaction

16

351 and decreased slightly with a longer reaction time (Appendix Fig. S7C). In contrast,

352 the Ba concentrations were high (11 to 20 mM) in solutions sampled after 1 minute of

353 reaction and decreased rapidly to a value below 1mM in increasing reaction time

354 (Appendix Fig. S7D), and the rapid Ba concentration drop was coincident with the

355 transformation of Ba-Mg amorphous carbonate. The concentration of Na, a

356 "conservative element" in this experimental system, remained constant throughout the

357 experiments at all temperatures (Appendix Fig. S7E). This indicates that the reaction

358 bottles were well sealed and there was a negligible loss of water vapor throughout the

359 experiments. In addition, the saturation index (SI) of norsethite decrease rapidly

360 (Appendix Fig. S7F) after 1 day for the experiment at 30°C and after 2 hours for

361 experiments from 40°C to 80°C and it corresponded to the transformation of Ba-Mg

362 AC to norsethite. Then the downward trend in Appendix Fig. S7F gradually slowed

363 down and the SI values became stabilized at around 1.5, a state of oversaturation for

364 norsethite.

365

366 **Mg isotope results**

367

368 In all experiments, $\delta^{26}Mg$ values of aqueous solutions were higher than those of the

369 solid products (Table 1 and Fig. 4A, B), corresponding to negative apparent Mg

370 isotope fractionation factors ($\Delta^{26}Mg_{solid-aq}$) (Fig.4C). Overall, the $\Delta^{26}Mg_{solid-aq}$ values

371 were positively related to the reaction temperature. For experiment Set I, the

372 $\Delta^{26}Mg_{solid-aq}$ between the freshly synthesized amorphous carbonate after 1 minute of

373 reaction and aqueous solution ranged from -0.83‰ at 30°C to -0.53‰ at 70°C, while

374 the formation of norsethite at 80°C resulted in a lower $\Delta^{26}Mg_{solid-aq}$ value (-1.27‰).

375 The transformation of the Ba-Mg amorphous carbonate after 2 hours of reaction time

376 was accompanied by a significant decrease in the $\Delta^{26}Mg_{solid-aq}$ values, which varied

377 from -1.83‰ at 40°C to -1.56‰ at 70ºC. For experiment at 30°C, the $\Delta^{26}Mg_{solid-aq}$

378 value remained nearly constant after 2 hours due to the lack of Ba-Mg amorphous

379 carbonate transformation, but after 1 day when the Ba-Mg amorphous carbonate was

380 transformed to norsethite, the $\Delta^{26}Mg_{solid-aq}$ decreased to -2.12‰.

381 .

382 One striking observation is that, after the complete transformation of Ba-Mg

383 amorphous carbonate to norsethite, the $\Delta^{26}Mg_{solid-aq}$ values began to increase

384 continuously with time, and spanned from -1.95‰ to -1.04‰ after 60 days of reaction.

385 Such increasing trend is confirmed in norsethite synthesis experiments Set II, in

386 which the apparent $\Delta^{26}Mg_{solid-aq}$ also increased from -1.39‰ at 40°C to –1.28‰ at 80°C

387 to -1.30‰ at 40°C to -0.73‰ at 80°C when the reaction time was extended to 276

388 days (Fig. 4D).

389

390 *ab initio* **calculation results**

391

392 The calculated volumes of norsethite, dolomite, and magnesite are 379.02, 330.83,

393 and 288.257Å^3, respectively (Table 2), which are about 3% larger than experimental

394 data (norsethite: 366.23Å3, Effenberger and Zemann, 1985; magnesite: 279.43Å3,

18

395   Markgraf and Reeder, 1985; dolomite: 320.20 Å3, Markgraf and Reeder, 1986), while

396   calculations using the two other functionals (LDA and PBE) predict smaller volumes.

397   The calculated average Mg-O bond length in norsethite, dolomite, and magnesite are

398   2.082, 2.111, and 2.126 Å, respectively.

399

400   The calculated temperature dependence of β-factor is shown in Appendix Fig. S6 and

401   the polynomial fitting ($10^3 \ln\beta = d \times 10^6 / T^2$) coefficients for norsethite, dolomite, and

402   magnesite are 1.9424, 1.8653, and 1.8177, respectively (Table 2). The calculation

403   results for two other functions are also listed. The calculated equilibrium fractionation

404   between magnesite and dolomite is -0.53‰ at 298K, which is consistent with Pinilla

405   et al. (2015) and Gao et al. (2018). The equilibrium Mg isotope fractionation between

406   norsethite and dolomite ($\alpha_{\text{nor-dolo}}$) can be calculated based on the calculated β-factors,

407   which followed a function of $10^3 \alpha_{\text{nor-dolo}} = -0.0771 \times 10^6 / T^2$. This function can be

408   combined with temperature-dependent function for Mg isotope fractionation between

409   dolomite and aqueous solution that was experimentally calibrated by Li et al. (2015),

410   which leads to temperature-dependent function for Mg isotope fractionation between

411   norsethite and aqueous solution (Fig. 5B):

412    $\Delta^{26}\text{Mg}_{\text{nor-aq}} = -0.0783 \times 10^6 / T^2$ (5)

413   where T is in Kevin (*K*).

414

415   DISCUSSIONS

416

19

417   Based on the experimental results in this study, the process of norsethite synthesis can

418   be generalized and separated into three stages (Fig.6), which are 1) the precipitation

419   of Ba-Mg AC, 2) the transformation of Ba-Mg amorphous carbonate to

420   nano-crystalline norsethite by fast dissolution-reprecipitation, and 3) recrystallization

421   of nano-norsethite by slow dissolution-reprecipitation. Different stages of norsethite

422   growth were accompanied by distinct Mg isotope fractionation behaviors. In

423   experiment Set I, the first solid phase to appear in experiments at 30°C to 70°C was

424   Ba-Mg amorphous carbonate only, despite that the initial mixed solution was highly

425   oversaturated to various Mg- and Ba- bearing minerals. This can be attributed to the

426   energy barrier for the formation of metastable amorphous carbonate being much lower

427   than the formation of crystalline minerals (Gebauer and Coelfen, 2011; Radha and

428   Navrotsky, 2013; Raiteri and Gale, 2010). The spherical morphology of Ba-Mg

429   amorphous carbonate as observed in this study is remarkably similar to that of the

430   synthesized amorphous calcium carbonate (ACC) reported in the literature (e.g., Xu et

431   al., 2004). It should be noted that the first solid phase that was sampled from the

432   experiment conducted at 80°C was a mixture of Ba-Mg amorphous carbonate and

433   nano-crystalline norsethite. This indicated that conversion of Ba-Mg amorphous

434   carbonate to norsethite was extremely fast at 80°C, occurring at a time scale similar to

435   experimental manipulation for solid separation (i.e., 1 minute). The $\Delta^{26}Mg_{solid-aq}$

436   between the amorphous carbonate after 1 minute of reaction and aqueous solution

437   ranged from -0.83‰ at 30°C to -0.53‰ at 70°C. Based on the calculation of

438   speciation of Mg^{2+} in aqueous solution and the Mg isotope fractionation factors

439   between different Mg species (Schott et al., 2016), the $\Delta^{26}Mg_{solid-Mg\_aq}$ between solid

440   products and free aqueous Mg^{2+} (refer to Mg^{2+} only bonded to H_2O molecules) ranged

441   from -0.54‰ at 30°C to -0.34‰ at 70°C (Appendix Table. S6). The small magnitude

442   of Mg isotope fractionation (-0.54‰ to -0.34‰) between amorphous carbonate and

443   free aqueous Mg^{2+} may indicate that the Mg^{2+} is incorporated into the amorphous

444   carbonate as the form of hydrated Mg.Actually the dehydration of metal ion would

445   lead to significant isotope fractionation (Hofmann et al., 2012) and this is consistent

446   with that the water content is positively correlated to the Mg content in amorphous

447   carbonate (Lin et al., 2015; Purgstaller et al., 2019).

448

449   The complete transformation of Ba-Mg amorphous carbonate to crystalline norsethite

450   occurred within 2 hours for experiments from 40°C to 80°C, while the Ba-Mg

451   amorphous carbonate persisted at 30°C until completely transformed to norsethite

452   after 1 day. This suggests that temperature exerts a primary control on the

453   transformation rate of amorphous carbonate for the norsethite synthesis experiments

454   in our study, which is consistent with the study of Liu and Li (2020). Based on XRD

455   analysis, norsethite is the only crystalline mineral phase after the transformation of

456   Ba-Mg amorphous carbonate (Appendix TableS2, Appendix Fig. S2). It should be

457   noted that other crystalline minerals, including northupite and witherite, have been

458   reported to the formation during the analogous synthesis experiments of norsethite

459   (Pimentel and Pina, 2014; Pimentel and Pina, 2016). The different reaction pathways

460   may be due to the different conditions used between these experiments. In this study,

461   the molar ratio of $(Mg^{2+} + Ba^{2+})$: CO_3^{2-} for reactants was above one, which means that

462   the available CO_3^{2-} was limited to form other carbonate minerals. By contrast, that

463   ratio was below one in the studies of Pimentel and Pina (2014; 2016). Additionally,

464   the saturation index (SI) for witherite and northupite were below zero after the

465   transformation of amorphous carbonate in this study (Appendix TableS4). This

466   suggests that the formation pathways could be variable and dependent on the solution

467   chemistry, as has been implied in previous studies on the transformation of

468   amorphous calcium carbonate (Lam et al., 2007; Loste et al., 2003; Purgstaller et al.,

469   2017; Rodriguez-Blanco et al., 2012). It is interesting to note that the norsethite

470   crystals obtained at 30°C showed more euhedral crystal morphology and larger crystal

471   size than that of norsethite obtained from 40°C to 70°C (Fig. 1B, Appendix Fig. S4).

472   During the crystal formation process, the crystal size is considered to be positively

473   correlated to the crystal growth rate, but negatively correlated to the crystal nucleation

474   rate. These two competing mechanisms ultimately determine the crystal size

475   distribution (Swanson, 1977). The transformation rate of Ba-Mg amorphous carbonate

476   for the experiment at 30°C was slower compared to transformation rates in

477   experiments at the higher temperatures (i.e., > 1 day versus < 2 hours), thus the

478   experiment 30°C should have been associated with slower nucleation rate, or less

479   norsethite crystal nucleus, which lead to the growth of larger crystals relative to

480   experiments at higher temperatures. The $\Delta^{26}Mg_{solid-aq}$ fractionation factors decreased

481   significantly during the transformation process (Fig. 4C, D). The remarkable decrease

482   in $\Delta^{26}Mg_{solid-aq}$ after complete transformation of Ba-Mg amorphous carbonate can be

22

483 attributed to the near-complete (100%) Mg isotope exchange during the

484 transformation process, which was rigorously proven using an enriched ^{25}Mg isotope

485 tracer (Liu and Li, 2020). However, it should be noted that the measured Δ^{26}Mg$_{solid-aq}$

486 factors for the newly formed nano-norsethite (-2.12‰ to -1.56‰) were significantly

487 lower than the calculated equilibrium Mg isotope fractionation factors for norsethite

488 (-0.68‰ to -0.50‰; Fig. 5B). This indicates that the Mg isotope fractionation during

489 a fast dissolution-reprecipitation process is kinetically controlled, which leads to

490 depletion in heavy Mg isotopes in the mineral phase.

491

492 After Ba-Mg amorphous carbonate transformation, recrystallization of the

493 nano-norsethite crystals proceeded with a longer reaction time. In this process, the

494 norsethite crystal coarsened and developed rhombohedra crystal habit, which was

495 accompanied by the disappearance of granular crystal shape (Fig. 2D~2I, Appendix

496 Fig S3~S4).The decrease of d(104) may reflect the increase of Mg: Ba ratio in the

497 norsethite, due to the larger ionic radius of Ba relative to Mg, similar to the case of

498 dolomite (Zhang et al., 2010). In the meantime, the FWHM of d(104) peak of the

499 norsethite decreased, pointing to better crystallinity of the mineral over time. It is

500 consistent with the common concept of recrystallization via Ostwald ripening during

501 mineral-fluid interaction (Ratke and Voorhees, 2002), which proceeds by a coupled

502 dissolution-reprecipitation mechanism, as evidenced by the continuous decrease of

503 SSA of solid products with longer reaction time (Fig.1B). The measured Δ^{26}Mg$_{solid-aq}$

504 factors increased with time for all experiments during this process (Fig. 4C, D) and

23

505   approached the calculated equilibrium fractionation factors, which implies that the

506   Mg exchange during this process was accompanied by the equilibrium fractionation.

507   It is in agreement with a general concept that a slow dissolution-reprecipitation would

508   drive the system to evolve towards equilibrium with time, as has been demonstrated in

509   experiments on multiple metal isotopes in carbonate minerals (Mavromatis et al.,

510   2017a; Mavromatis et al., 2016; Oelkers et al., 2018; Oelkers et al., 2019; Pearce et al.,

511   2012) and Mg isotopes for Mg-sulfate (Li et al., 2011). In addition to the

512   dissolution-reprecipitation, the Mg isotope composition of minerals may be changed

513   via the surface exchange or diffusion process (e.g, Huang et al., 2010; Richter et al.,

514   2003; Richter et al., 2008; Teng et al., 2011). However, based on the SSA value, the

515   calculated total amount of Mg at the surface only accounts for less than 3% of the

516   total Mg in norsethite crystals (details in Appendix). Therefore, the surface process is

517   not responsible for the significant increase of the δ^{26}Mg of norsethite. Moreover,

518   diffusion of Mg ion in carbonate (Fisler and Cygan, 1999; Kent et al., 2001) is too

519   slow at the experimental temperatures in this study to influence the Mg isotope

520   composition of norsethite (details in Appendix). Furthermore, the slight decreased Mg

521   concentration during this process indicate the extra Mg mass transfer from solution to

522   the solid phase, which can lead to the extra Mg isotope fractionation. Therefore, the

523   mass transfer corrections were conducted (detail in Appendix). This correction had

524   limited influence on the increasing trend of Mg isotope fractionation with longer

525   reaction time (Appendix Fig. S9).Notably, the magnitude of the increase in

526   Δ^{26}Mg$_{solid-aq}$ fractionation factors was greater for the experiments at higher

527   temperatures, irrespective of experimental settings (experiment set I or set II; Fig. 5A).

528   This is attributed to continuous isotope exchange between norsethite crystals and

529   aqueous solution in this stage, as exchange rates in reactions are positively

530   temperature-dependent (Li et al., 2015).

531

532   IMPLICATIONS

533

534   Magnesium isotopes in marine carbonate have been applied to reconstruct the Mg

535   isotopic and chemical composition of ancient seawater (Crockford et al., 2020; Fantle

536   and Higgins, 2014; Gothmann et al., 2017; Higgins and Schrag, 2012; Hu et al., 2019;

537   Li et al., 2015; Li et al., 2019; Pogge von Strandmann et al., 2014). However, the use

538   of carbonates as Mg isotope archive of seawater faces several challenges, including :

539   (1) to discern whether isotope equilibrium fractionation has been attained between the

540   carbonate and seawater; (2) to ascertain whether the Mg isotope records in carbonate

541   are influenced by the post-depositional process. Our findings show that significant

542   exchange of Mg between solid and solution occurs during recrystallization of

543   norsethite via dissolution-reprecipitation, leading to the obvious alteration of Mg

544   isotopic compositions. However, the incorporation of aqueous Mg^{2+} into carbonate

545   minerals was not supported under ambient temperature due to the kinetic barrier of

546   dehydration (Land, 1998) and the dolomite precipitation is rare in the modern

547   sedimentary environment (Warren, 2000). By contrast, massive dolomite formation

548   was found in the geological record (Burns et al., 2000; Given and Wilkinson, 1987),

549   which demonstrated that the Mg content and isotope composition of carbonate could

550   be influenced by post-depositional processes. Meanwhile, the extent to the alteration

551   of carbonate isotope composition is influenced by the reaction rate, duration of

552   reaction, and the degree of isotopic disequilibrium (Chanda and Fantle, 2017; Fantle,

553   2015; Fantle et al., 2020; Huber et al., 2017). Therefore, various geological settings

554   and post-depositional history of samples should be taken into consideration to have

555   the potential impact the recrystallization on Mg isotopic record in carbonates. For

556   example, if a carbonate of marine origin remained in contact with seawater (i.e.,

557   "seawater buffered") for a protracted period of time, the continuous isotope exchange

558   shall result in the Mg isotope re-equilibrium between carbonate and coeval seawater,

559   therefore, seawater Mg isotope composition can be recorded (Li et al., 2015).

560   However, sedimentary carbonates also underwent burial and related post-depositional

561   processes, during which they reacted with isotopically evolved pore water or

562   hydrothermal fluids, leading to further isotope exchange. If that the fluids contain

563   insufficient Mg relative to the carbonate, which is a so-called "sediment-buffered"

564   environment, slow recrystallization of carbonate would take place, but the process

565   will reset the Mg isotope composition of fluids rather than that of Mg-rich carbonates.

566   It is a common case for carbon isotopes in carbonates (Swart, 2015) but also for Mg

567   isotopes in dolostone during the burial metamorphism (Azmy et al., 2013; Geske et al.,

568   2012; Hu et al., 2017) or hydrothermal alteration(Geske et al., 2015; Hu et al., 2019).

569

570   A "fluid-buffered" situation could also take place for some carbonates during burial

571   and subsequent post-depositional processes. If the amount of Mg in fluids was

572   sufficient enough, the recrystallization would cause overprinting of Mg isotope

573   signatures of carbonate while that of fluids evolves synchronously or remains

574   relatively constant (e.g., Fantle and Higgins, 2014; Huang et al., 2015). The greatest

575   challenge in metal isotope studies of carbonate archives lies in distinguishing

576   "sediment-buffered" and "fluid-buffered" situations, which would require applications

577   of multiple geochemical tools to interrogate the fidelity of Mg isotopes in the studied

578   carbonates (Riechelmann et al., 2020).

579

580   Our results provide new insights for applications of Mg isotopes in the carbonate

581   archive. On the one hand, our study indicates that the amorphous carbonate

582   transformation can lead to significant decrease of Mg isotope fractionation between

583   solid and solution phase. As a consequence, the Mg isotope fractionation between the

584   newly formed crystalline carbonate minerals and surrounding solution could be more

585   negative than equilibrium values from a single-stage precipitation, thus special

586   attention is required in Mg isotope studies on biogenic carbonates. On the other hand,

587   the recrystallization has a great impact on the preservation of the initial isotope

588   signature of crystalline carbonate, the extent to which this may influence the original

589   isotopic signature depends on the type of diagenetic fluids and the relative Mg amount

590   of carbonate and fluids.

591

592   ACKOWLEDEGMENTS

593

604

605   REFERENCE CITED

606   Azmy, K., Lavoie, D., Wang, Z., Brand, U., Al-Aasm, I., Jackson, S., and Girard, I. (2013)
607   Magnesium-isotope and REE compositions of Lower Ordovician carbonates from eastern
608   Laurentia: Implications for the origin of dolomites and limestones. Chemical Geology, 356,
609   64-75.

610   Banner, J.L. (1995) Application of the trace-element and isotope geochemistry of strontium to studies
611   of carbonate diagenesis. Sedimentology, 42(5), 805-824.

612   Baronnet, A., Cuif, J.P., Dauphin, Y., Farre, B., and Nouet, J. (2008) Crystallization of biogenic
613   Ca-carbonate within organo-mineral micro-domains. Structure of the calcite prisms of the
614   Pelecypod Pinctada margaritifera (Mollusca) at the submicron to nanometre ranges.
615   Mineralogical Magazine, 72(2), 617-626.

616   Bialik, O.M., Wang, X., Zhao, S., Waldmann, N.D., Frank, R., and Li, W. (2018) Mg isotope response to
617   dolomitization in hinterland-attached carbonate platforms: Outlook of δ^{26}Mg as a tracer of
618   basin restriction and seawater Mg/Ca ratio. Geochimica Et Cosmochimica Acta, 235, 189-207.

619   Bice, K.L., Birgel, D., Meyers, P.A., Dahl, K.A., Hinrichs, K.U., and Norris, R.D. (2006) A multiple proxy
620   and model study of Cretaceous upper ocean temperatures and atmospheric CO2
621   concentrations. Paleoceanography, 21(2).

622   Bigeleisen, J., and Mayer, M.G. (1947) Calculation of equilibrium constants for isotopic exchange
623   reactions. Journal of Chemical Physics, 15(5), 261-267.

624 Børja, I., and Nilsen, P. (2009) Long term effect of liming and fertilization on ectomycorrhizal
625   colonization and tree growth in old Scots pine (Pinus sylvestris L.) stands. Plant and Soil,
626   314(1), 109-119.

627 Burdige, D.J., Hu, X., and Zimmerman, R.C. (2010) The widespread occurrence of coupled carbonate
628   dissolution/reprecipitation in surface sediments on the Bahamas Bank. American Journal of
629   Science, 310(6), 492.

630 Burns, S.J., McKenzie, J.A., and Vasconcelos, C. (2000) Dolomite formation and biogeochemical cycles
631   in the Phanerozoic. Sedimentology, 47, 49-61.

632 Chanda, P., and Fantle, M.S. (2017) Quantifying the effect of diagenetic recrystallization on the Mg
633   isotopic composition of marine carbonates. Geochimica Et Cosmochimica Acta, 204, 219-239.

634 Chanda, P., Gorski, C.A., Oakes, R.L., and Fantle, M.S. (2019) Low temperature stable mineral
635   recrystallization of foraminiferal tests and implications for the fidelity of geochemical proxies.
636   Earth and Planetary Science Letters, 506, 428-440.

637 Crockford, P.W., Kunzmann, M., Blättler, C.L., Kalderon-Asael, B., Murphy, J.G., Ahm, A.-S., Sharoni, S.,
638   Halverson, G.P., Planavsky, N.J., Halevy, I., and Higgins, J.A. (2020) Reconstructing
639   Neoproterozoic seawater chemistry from early diagenetic dolomite. Geology.

640 Davis, K.J., Dove, P.M., and De Yoreo, J.J. (2000) The role of Mg^{2+} as an impurity in calcite growth.
641   Science, 290(5494), 1134-1137.

642 De Muynck, W., Debrouwer, D., De Belie, N., and Verstraete, W. (2008) Bacterial carbonate
643   precipitation improves the durability of cementitious materials. Cement and Concrete
644   Research, 38(7), 1005-1014.

645 De Yoreo, J.J., Waychunas, G.A., Jun, Y.-S., and Fernandez-Martinez, A. (2013) In situ Investigations of
646   Carbonate Nucleation on Mineral and Organic Surfaces. Reviews in Mineralogy and
647   Geochemistry, 77(1), 229-257.

648 Derry, L.A., Kaufman, A.J., and Jacobsen, S.B. (1992) Sedimentary cycling and environmental change in
649   the Late Proterozoic: Evidence from stable and radiogenic isotopes. Geochimica et
650   Cosmochimica Acta, 56(3), 1317-1329.

651 Effenberger, H., Pippinger, T., Libowitzky, E., Lengauer, C.L., and Miletich, R. (2014) Synthetic norsethite,
652   BaMg(CO3)(2): revised crystal structure, thermal behaviour and displacive phase transition.
653   Mineralogical Magazine, 78(7), 1589-1611.

654 Effenberger, H., and Zemann, J. (1985) Single-crystal x-ray-investigation of norsethite, $BaMg(CO_3)_2$ -
655   one more mineral with an aplanar carbonate group. Zeitschrift Fur Kristallographie, 171(3-4),
656   275-280.

657 Fantle, M.S. (2015) Calcium isotopic evidence for rapid recrystallization of bulk marine carbonates and
658   implications for geochemical proxies. Geochimica et Cosmochimica Acta, 148, 378-401.

659 Fantle, M.S., Barnes, B.D., and Lau, K.V. (2020) The Role of Diagenesis in Shaping the Geochemistry of
660   the Marine Carbonate Record. Annual Review of Earth and Planetary Sciences, 48(1),
661   549-583.

662 Fantle, M.S., and Higgins, J. (2014) The effects of diagenesis and dolomitization on Ca and Mg isotopes
663   in marine platform carbonates: Implications for the geochemical cycles of Ca and Mg.
664   Geochimica Et Cosmochimica Acta, 142, 458-481.

665 Fisler, D.K., and Cygan, R.T. (1999) Diffusion of Ca and Mg in calcite. American Mineralogist, 84(9),
666   1392-1399.

667 Frierdich, A.J., Nebel, O., Beard, B.L., and Johnson, C.M. (2019) Iron isotope exchange and

29

668   fractionation between hematite (α-Fe$_2$O$_3$) and aqueous Fe(II): A combined three-isotope and
669   reversal-approach to equilibrium study. Geochimica et Cosmochimica Acta, 245, 207-221.
670 Gao, C., Cao, X., Liu, Q., Yang, Y., Zhang, S., He, Y., Tang, M., and Liu, Y. (2018) Theoretical calculation of
671   equilibrium Mg isotope fractionations between minerals and aqueous solutions. Chemical
672   Geology, 488, 62-75.
673 Gautier, Q., Bénézeth, P., Mavromatis, V., and Schott, J. (2014) Hydromagnesite solubility product and
674   growth kinetics in aqueous solution from 25 to 75°C. Geochimica et Cosmochimica Acta, 138,
675   1-20.
676 Gebauer, D., and Coelfen, H. (2011) Prenucleation clusters and non-classical nucleation. Nano Today,
677   6(6), 564-584.
678 Geske, A., Goldstein, R.H., Mavromatis, V., Richter, D.K., Buhl, D., Kluge, T., John, C.M., and
679   Immenhauser, A. (2015) The magnesium isotope (δ^{26}Mg) signature of dolomites. Geochimica
680   et Cosmochimica Acta, 149, 131-151.
681 Geske, A., Zorlu, J., Richter, D.K., Buhl, D., Niedermayr, A., and Immenhauser, A. (2012) Impact of
682   diagenesis and low grade metamorphism on isotope (delta(26)mg, delta C-13, delta O-18 and
683   Sr-87/Sr-86) and elemental (Ca, Mg, Mn, Fe and Sr) signatures of Triassic sabkha dolomites.
684   Chemical Geology, 332, 45-64.
685 Giuffre, A.J., Gagnon, A.C., De Yoreo, J.J., and Dove, P.M. (2015) Isotopic tracer evidence for the
686   amorphous calcium carbonate to calcite transformation by dissolution-reprecipitation.
687   Geochimica Et Cosmochimica Acta, 165, 407-417.
688 Given, R.K., and Wilkinson, B.H. (1987) Dolomite abundance and stratigraphic age; constraints on rates
689   and mechanisms of Phanerozoic dolostone formation. Journal of Sedimentary Research,
690   57(6), 1068-1078.
691 Gorski, C.A., and Fantle, M.S. (2017) Stable mineral recrystallization in low temperature aqueous
692   systems: A critical review. Geochimica et Cosmochimica Acta, 198, 439-465.
693 Gothmann, A.M., Stolarski, J., Adkins, J.F., and Higgins, J.A. (2017) A Cenozoic record of seawater Mg
694   isotopes in well-preserved fossil corals. Geology, 45(11), 1039-1042.
695 Gower, L.B. (2008) Biomimetic Model Systems for Investigating the Amorphous Precursor Pathway and
696   Its Role in Biomineralization. Chemical Reviews, 108(11), 4551-4627.
697 Gu, C., Li, Q., Gu, Z., and Zhu, G. (2008) Study on application of CeO2 and CaCO3 nanoparticles in
698   lubricating oils. Journal of Rare Earths, 26(2), 163-167.
699 Harrison, A.L., Mavromatis, V., Oelkers, E.H., and Bénézeth, P. (2019) Solubility of the hydrated
700   Mg-carbonates nesquehonite and dypingite from 5 to 35 °C: Implications for CO2 storage and
701   the relative stability of Mg-carbonates. Chemical Geology, 504, 123-135.
702 Higgins, J.A., and Schrag, D.P. (2012) Records of Neogene seawater chemistry and diagenesis in
703   deep-sea carbonate sediments and pore fluids. Earth and Planetary Science Letters, 357,
704   386-396.
705 Hofmann, A.E., Bourg, I.C., and DePaolo, D.J. (2012) Ion desolvation as a mechanism for kinetic isotope
706   fractionation in aqueous systems. Proceedings of the National Academy of Sciences of the
707   United States of America, 109(46), 18689-18694.
708 Hong, M., Xu, J., and Teng, H.H. (2016) Evolution of calcite growth morphology in the presence of
709   magnesium: Implications for the dolomite problem. Geochimica et Cosmochimica Acta, 172,
710   55-64.
711 Hu, X., and Burdige, D.J. (2007) Enriched stable carbon isotopes in the pore waters of carbonate

712   sediments dominated by seagrasses: Evidence for coupled carbonate dissolution and
713   reprecipitation. Geochimica et Cosmochimica Acta, 71(1), 129-144.

714 Hu, Z., Hu, W., Liu, C., Sun, F., Liu, Y., and Li, W. (2019) Conservative behavior of Mg isotopes in massive
715   dolostones: From diagenesis to hydrothermal reworking. Sedimentary Geology, 381, 65-75.

716 Hu, Z., Hu, W., Wang, X., Lu, Y., Wang, L., Liao, Z., and Li, W. (2017) Resetting of Mg isotopes between
717   calcite and dolomite during burial metamorphism: Outlook of Mg isotopes as
718   geothermometer and seawater proxy. Geochimica et Cosmochimica Acta, 208, 24-40.

719 Huang, F., Chakraborty, P., Lundstrom, C.C., Holmden, C., Glessner, J.J.G., Kieffer, S.W., and Lesher, C.E.
720   (2010) Isotope fractionation in silicate melts by thermal diffusion. Nature, 464, 396.

721 Huang, K.-J., Shen, B., Lang, X.-G., Tang, W.-B., Peng, Y., Ke, S., Kaufman, A.J., Ma, H.-R., and Li, F.-B.
722   (2015) Magnesium isotopic compositions of the Mesoproterozoic dolostones: Implications for
723   Mg isotopic systematics of marine carbonates. Geochimica Et Cosmochimica Acta, 164,
724   333-351.

725 Huber, C., Druhan, J.L., and Fantle, M.S. (2017) Perspectives on geochemical proxies: The impact of
726   model and parameter selection on the quantification of carbonate recrystallization rates.
727   Geochimica et Cosmochimica Acta, 217, 171-192.

728 Jacob, D.E., Wirth, R., Agbaje, O.B.A., Branson, O., and Eggins, S.M. (2017) Planktic foraminifera form
729   their shells via metastable carbonate phases. Nature Communications, 8(1), 1265.

730 Jin, D., and Yue, L. (2008) Tribological properties study of spherical calcium carbonate composite as
731   lubricant additive. Materials Letters, 62(10), 1565-1568.

732 Kent, A.J.R., Hutcheon, I.D., Ryerson, F.J., and Phinney, D.L. (2001) The temperature of formation of
733   carbonate in martian meteorite ALH84001: constraints from cation diffusion11Associate
734   editor: H. E. Newsom. Geochimica et Cosmochimica Acta, 65(2), 311-321.

735 Kresse, G., and Joubert, D. (1999) From ultrasoft pseudopotentials to the projector augmented-wave
736   method. Physical Review B, 59(3), 1758-1775.

737 Lachniet, M.S. (2009) Climatic and environmental controls on speleothem oxygen-isotope values.
738   Quaternary Science Reviews, 28(5), 412-432.

739 Lam, R.S.K., Charnock, J.M., Lennie, A., and Meldrum, F.C. (2007) Synthesis-dependant structural
740   variations in amorphous calcium carbonate. Crystengcomm, 9(12), 1226-1236.

741 Land, L.S. (1998) Failure to precipitate dolomite at 25°C from dilute solution despite 1000-fold
742   oversaturation after 32 years. Aquatic Geochemistry, 4(3-4), 361-368.

743 Li, W., Beard, B.L., and Johnson, C.M. (2011) Exchange and fractionation of Mg isotopes between
744   epsomite and saturated $MgSO_4$ solution. Geochimica Et Cosmochimica Acta, 75(7),
745   1814-1828.

746 Li, W., Beard, B.L., Li, C., Xu, H., and Johnson, C.M. (2015) Experimental calibration of Mg isotope
747   fractionation between dolomite and aqueous solution and its geological implications.
748   Geochimica Et Cosmochimica Acta, 157, 164-181.

749 Li, W., Bialik, O.M., Wang, X., Yang, T., Hu, Z., Huang, Q., Zhao, S., and Waldmann, N.D. (2019) Effects of
750   early diagenesis on Mg isotopes in dolomite: The roles of Mn(IV)-reduction and
751   recrystallization. Geochimica et Cosmochimica Acta, 250, 1-17.

752 Lin, C.-J., Yang, S.-Y., Huang, S.-J., and Chan, J.C.C. (2015) Structural Characterization of Mg-Stabilized
753   Amorphous Calcium Carbonate by Mg-25 Solid-State NMR Spectroscopy. Journal of Physical
754   Chemistry C, 119(13), 7225-7233.

755 Lindner, M., and Jordan, G. (2018) On the growth of witherite and its replacement by the Mg-bearing

756   double carbonate norsethite: Implications for the dolomite problem. American Mineralogist,

757   103(2), 252-259.

758 Lindner, M., Saldi, G.D., Carrocci, S., Benezeth, P., Schott, J., and Jordan, G. (2018) On the growth of

759   anhydrous Mg-bearing carbonates - Implications from norsethite growth kinetics. Geochimica

760   Et Cosmochimica Acta, 238, 424-437.

761 Liu, C., and Li, W. (2020) Transformation of amorphous precursor to crystalline carbonate: Insights

762   from Mg isotopes in the dolomite-analogue mineral norsethite [$BaMg(CO_3)_2$]. Geochimica et

763   Cosmochimica Acta, 272, 1-20.

764 Liu, C., Wang, Z., and Macdonald, F.A. (2018) Sr and Mg isotope geochemistry of the basal Ediacaran

765   cap limestone sequence of Mongolia: Implications for carbonate diagenesis, mixing of glacial

766   meltwaters, and seawater chemistry in the aftermath of Snowball Earth. Chemical Geology,

767   491, 1-13.

768 Loste, E., Wilson, R.M., Seshadri, R., and Meldrum, F.C. (2003) The role of magnesium in stabilising

769   amorphous calcium carbonate and controlling calcite morphologies. Journal of Crystal

770   Growth, 254(1-2), 206-218.

771 Markgraf, S.A., and Reeder, R.J. (1985) High-temperature structure refinements of calcite and

772   magnesite. American Mineralogist, 70(5-6), 590-600.

773 -. (1986) High-temperature crystal chemistry of dolomite. American Mineralogist, 71, 795-804.

774 Mass, T., Giuffre, A.J., Sun, C.-Y., Stifler, C.A., Frazier, M.J., Neder, M., Tamura, N., Stan, C.V., Marcus,

775   M.A., and Gilbert, P.U.P.A. (2017) Amorphous calcium carbonate particles form coral

776   skeletons. Proceedings of the National Academy of Sciences of the United States of America,

777   114(37), E7670-E7678.

778 Mavromatis, V., Harrison, A.L., Eisenhauer, A., and Dietzel, M. (2017a) Strontium isotope fractionation

779   during strontianite ($SrCO_3$) dissolution, precipitation and at equilibrium. Geochimica Et

780   Cosmochimica Acta, 218, 201-214.

781 Mavromatis, V., Purgstaller, B., Dietzel, M., Buhl, D., Immenhauser, A., and Schott, J. (2017b) Impact of

782   amorphous precursor phases on magnesium isotope signatures of Mg-calcite. Earth and

783   Planetary Science Letters, 464, 227-236.

784 Mavromatis, V., van Zuilen, K., Purgstaller, B., Baldermann, A., Nagler, T.F., and Dietzel, M. (2016)

785   Barium isotope fractionation during witherite ($BaCO_3$) dissolution, precipitation and at

786   equilibrium. Geochimica Et Cosmochimica Acta, 190, 72-84.

787 McDermott, F. (2004) Palaeo-climate reconstruction from stable isotope variations in speleothems: a

788   review. Quaternary Science Reviews, 23(7), 901-918.

789 Mitsuguchi, T., Matsumoto, E., Abe, O., Uchida, T., and Isdale, P.J. (1996) Mg/Ca Thermometry in Coral

790   Skeletons. Science, 274(5289), 961.

791 Monkhorst, H.J., and Pack, J.D. (1976) Special points for Brillouin-zone integrations. Physical Review B,

792   13(12), 5188-5192.

793 Mor Khalifa, G., Kahil, K., Erez, J., Kaplan Ashiri, I., Shimoni, E., Pinkas, I., Addadi, L., and Weiner, S.

794   (2018) Characterization of unusual MgCa particles involved in the formation of foraminifera

795   shells using a novel quantitative cryo SEM/EDS protocol. Acta Biomaterialia, 77, 342-351.

796 Morse, J.W., and Mackenzie, F.T. (1990) Geochemistry of Sedimentary Carbonates. 706 p. Elsevier

797   Science.

798 Nielsen, M.R., Sand, K.K., Rodriguez-Blanco, J.D., Bovet, N., Generosi, J., Dalby, K.N., and Stipp, S.L.S.

799   (2016) Inhibition of Calcite Growth: Combined Effects of Mg2+ and SO42−. Crystal Growth &

800   Design, 16(11), 6199-6207.

801   Oelkers, E.H., Berninger, U.-N., Perez-Fernandez, A., Chmeleff, J., and Mavromatis, V. (2018) The
802   temporal evolution of magnesium isotope fractionation during hydromagnesite dissolution,
803   precipitation, and at equilibrium. Geochimica Et Cosmochimica Acta, 226, 36-49.

804   Oelkers, E.H., von Strandmann, P.A.E.P., and Mavromatis, V. (2019) The rapid resetting of the Ca
805   isotopic signatures of calcite at ambient temperature during its congruent dissolution,
806   precipitation, and at equilibrium. Chemical Geology, 512, 1-10.

807   Pearce, C.R., Saldi, G.D., Schott, J., and Oelkers, E.H. (2012) Isotopic fractionation during congruent
808   dissolution, precipitation and at equilibrium: Evidence from Mg isotopes. Geochimica Et
809   Cosmochimica Acta, 92, 170-183.

810   Perdew, J.P., Burke, K., and Ernzerhof, M. (1996) Generalized gradient approximation made simple.
811   Physical Review Letters, 77(18), 3865-3868.

812   Perdew, J.P., Ruzsinszky, A., Csonka, G.I., Vydrov, O.A., Scuseria, G.E., Constantin, L.A., Zhou, X., and
813   Burke, K. (2008) Restoring the density-gradient expansion for exchange in solids and surfaces.
814   Phys Rev Lett, 100(13), 136406.

815   Perdew, J.P., and Zunger, A. (1981) Self-interaction correction to density-functional approximations for
816   many-electron systems. Physical Review B, 23(10), 5048-5079.

817   Pimentel, C., and Pina, C.M. (2014) The formation of the dolomite-analogue norsethite: Reaction
818   pathway and cation ordering. Geochimica Et Cosmochimica Acta, 142, 217-223.

819   -. (2016) Reaction pathways towards the formation of dolomite-analogues at ambient conditions.
820   Geochimica Et Cosmochimica Acta, 178, 259-267.

821   Pimentel, C., Pina, C.M., and Sainz-Díaz, C.I. (2021) DFT Simulations of the Structure and Cation Order
822   of Norsethite, BaMg(CO3)2. ACS Earth and Space Chemistry.

823   Pinilla, C., Blanchard, M., Balan, E., Natarajan, S.K., Vuilleumier, R., and Mauri, F. (2015) Equilibrium
824   magnesium isotope fractionation between aqueous Mg2+ and carbonate minerals: Insights
825   from path integral molecular dynamics (vol 163, pg 126, 2015). Geochimica Et Cosmochimica
826   Acta, 167, 313-314.

827   Pogge von Strandmann, P.A.E., Forshaw, J., and Schmidt, D.N. (2014) Modern and Cenozoic records of
828   seawater magnesium from foraminiferal Mg isotopes. Biogeosciences, 11(18), 5155-5168.

829   Politi, Y., Metzler, R.A., Abrecht, M., Gilbert, B., Wilt, F.H., Sagi, I., Addadi, L., Weiner, S., and Gilbert,
830   P.U.P.A. (2008) Transformation mechanism of amorphous calcium carbonate into calcite in
831   the sea urchin larval spicule (vol 105, pg 17362, 2008). Proceedings of the National Academy
832   of Sciences of the United States of America, 105(50), 20045-20045.

833   Purgstaller, B., Goetschl, K.E., Mavromatis, V., and Dietzel, M. (2019) Solubility investigations in the
834   amorphous calcium magnesium carbonate system. Crystengcomm, 21(1), 155-164.

835   Purgstaller, B., Konrad, F., Dietzel, M., Immenhauser, A., and Mavromatis, V. (2017) Control of
836   Mg^{2+}/Ca^{2+} Activity Ratio on the Formation of Crystalline Carbonate Minerals via an
837   Amorphous Precursor. Crystal Growth & Design, 17(3), 1069-1078.

838   Purgstaller, B., Mavromatis, V., Immenhauser, A., and Dietzel, M. (2016) Transformation of Mg-bearing
839   amorphous calcium carbonate to Mg-calcite - In situ monitoring. Geochimica Et
840   Cosmochimica Acta, 174, 180-195.

841   Radha, A.V., and Navrotsky, A. (2013) Thermodynamics of Carbonates. Reviews in Mineralogy and
842   Geochemistry, 77(1), 73-121.

843   Rae, J.W.B., Foster, G.L., Schmidt, D.N., and Elliott, T. (2011) Boron isotopes and B/Ca in benthic

844   foraminifera: Proxies for the deep ocean carbonate system. Earth and Planetary Science
845   Letters, 302(3), 403-413.
846 Raiteri, P., and Gale, J.D. (2010) Water Is the Key to Nonclassical Nucleation of Amorphous Calcium
847   Carbonate. Journal of the American Chemical Society, 132(49), 17623-17634.
848 Ratke, L., and Voorhees, P.W. (2002) Growth and Coarsening Ostwald Ripening in Material Processing.
849   298 p. Springer, Berlin, Heidelberg.
850 Raz, S., Hamilton, P.C., Wilt, F.H., Weiner, S., and Addadi, L. (2003) The transient phase of amorphous
851   calcium carbonate in sea urchin larval spicules: The involvement of proteins and magnesium
852   ions in its formation and stabilization. Advanced Functional Materials, 13(6), 480-486.
853 Reeves, D., and Rothman, D.H. (2013) Age dependence of mineral dissolution and precipitation rates.
854   Global Biogeochemical Cycles, 27(3), 906-919.
855 Richter, F.M., Davis, A.M., DePaolo, D.J., and Watson, E.B. (2003) Isotope fractionation by chemical
856   diffusion between molten basalt and rhyolite. Geochimica et Cosmochimica Acta, 67(20),
857   3905-3923.
858 Richter, F.M., Watson, E.B., Mendybaev, R.A., Teng, F.-Z., and Janney, P.E. (2008) Magnesium isotope
859   fractionation in silicate melts by chemical and thermal diffusion. Geochimica et
860   Cosmochimica Acta, 72(1), 206-220.
861 Riechelmann, S., Mavromatis, V., Buhl, D., Dietzel, M., and Immenhauser, A. (2020) Controls on
862   formation and alteration of early diagenetic dolomite: A multi-proxy δ44/40Ca, δ26Mg, δ18O
863   and δ13C approach. Geochimica et Cosmochimica Acta, 283, 167-183.
864 Ries, J.B. (2004) Effect of ambient Mg/Ca ratio on Mg fractionation in calcareous marine invertebrates:
865   A record of the oceanic Mg/Ca ratio over the Phanerozoic. Geology, 32(11), 981-984.
866 Rodriguez-Blanco, J.D., Sand, K.K., and Benning, L.G. (2017) ACC and Vaterite as Intermediates in the
867   Solution-Based Crystallization of CaCO3. In A.E.S. Van Driessche, M. Kellermeier, L.G. Benning,
868   and D. Gebauer, Eds. New Perspectives on Mineral Nucleation and Growth: From Solution
869   Precursors to Solid Materials, p. 93-111. Springer International Publishing, Cham.
870 Rodriguez-Blanco, J.D., Shaw, S., Bots, P., Roncal-Herrero, T., and Benning, L.G. (2012) The role of pH
871   and Mg on the stability and crystallization of amorphous calcium carbonate. Journal of Alloys
872   and Compounds, 536, S477-S479.
873 Rollion-Bard, C., Blamart, D., Trebosc, J., Tricot, G., Mussi, A., and Cuif, J.-P. (2011) Boron isotopes as
874   pH proxy: A new look at boron speciation in deep-sea corals using 11B MAS NMR and EELS.
875   Geochimica et Cosmochimica Acta, 75(4), 1003-1012.
876 Schott, J., Mavromatis, V., Fujii, T., Pearce, C.R., and Oelkers, E.H. (2016) The control of carbonate
877   mineral Mg isotope composition by aqueous speciation: Theoretical and experimental
878   modeling. Chemical Geology, 445, 120-134.
879 Sun, C.-Y., Stifler, C.A., Chopdekar, R.V., Schmidt, C.A., Parida, G., Schoeppler, V., Fordyce, B.I., Brau, J.H.,
880   Mass, T., Tambutté, S., and Gilbert, P.U.P.A. (2020) From particle attachment to space-filling
881   coral skeletons. Proceedings of the National Academy of Sciences, 202012025.
882 Sun, Z.M., Lu, X.C., Jia, X.C., Bai, Y.S., and Hu, W.X. (2017) Optimization of Mercury Intrusion Capillary
883   Pressure Measurement for Characterizing the Pore Structure of Tight Rocks. Journal of
884   Nanoscience and Nanotechnology, 17(9), 6242-6251.
885 Swanson, S.E. (1977) Relation of nucleation and crystal-growth rate to the development of granitic
886   textures. American Mineralogist, 62(9-10), 966-978.
887 Swart, P.K. (2015) The geochemistry of carbonate diagenesis: The past, present and future.

888   Sedimentology, 62(5), 1233-1304.

889   Teng, F.-Z., Dauphas, N., Helz, R.T., Gao, S., and Huang, S. (2011) Diffusion-driven magnesium and iron
890   isotope fractionation in Hawaiian olivine. Earth and Planetary Science Letters, 308(3),
891   317-324.

892   Teng, H.H., Dove, P.M., and De Yoreo, J.J. (2000) Kinetics of calcite growth: surface processes and
893   relationships to macroscopic rate laws. Geochimica et Cosmochimica Acta, 64(13),
894   2255-2266.

895   Togo, A., and Tanaka, I. (2015) First principles phonon calculations in materials science. Scripta
896   Materialia, 108, 1-5.

897   Urey, H.C. (1947) The thermodynamic properties of isotopic substances. Journal of the Chemical
898   Society(MAY), 562-581.

899   Von Euw, S., Zhang, Q., Manichev, V., Murali, N., Gross, J., Feldman, L.C., Gustafsson, T., Flach, C.,
900   Mendelsohn, R., and Falkowski, P.G. (2017) Biological control of aragonite formation in stony
901   corals. Science, 356(6341), 933.

902   Wang, Y., Yao, Z., Zhan, Y., Zheng, X., Zhou, M., Yan, G., Wang, L., Werner, C., and Butterbach-Bahl, K.
903   (2021) Potential benefits of liming to acid soils on climate change mitigation and food security.
904   Global Change Biology, 27(12), 2807-2821.

905   Wang, Y.J., Cheng, H., Edwards, R.L., An, Z.S., Wu, J.Y., Shen, C.C., and Dorale, J.A. (2001) A
906   High-Resolution Absolute-Dated Late Pleistocene Monsoon Record from Hulu Cave, China.
907   Science, 294(5550), 2345-2348.

908   Warren, J. (2000) Dolomite: occurrence, evolution and economically important associations.
909   Earth-Science Reviews, 52(1-3), 1-81.

910   Weiss, I.M., Tuross, N., Addadi, L., and Weiner, S. (2002) Mollusc larval shell formation: Amorphous
911   calcium carbonate is a precursor phase for aragonite. Journal of Experimental Zoology, 293(5),
912   478-491.

913   Xu, X.R., Han, J.T., and Cho, K. (2004) Formation of amorphous calcium carbonate thin films and their
914   role in biomineralization. Chemistry of Materials, 16(9), 1740-1746.

915   Zamanian, K., Pustovoytov, K., and Kuzyakov, Y. (2016) Recrystallization of shell carbonate in soil: 14C
916   labeling, modeling and relevance for dating and paleo-reconstructions. Geoderma, 282,
917   87-95.

918   Zhang, F., Algeo, T.J., Romaniello, S.J., Cui, Y., Zhao, L., Chen, Z.-Q., and Anbar, A.D. (2018) Congruent
919   Permian-Triassic δ238U records at Panthalassic and Tethyan sites: Confirmation of
920   global-oceanic anoxia and validation of the U-isotope paleoredox proxy. Geology, 46(4),
921   327-330.

922   Zhang, F., Xu, H., Konishi, H., and Roden, E.E. (2010) A relationship between d(104) value and
923   composition in the calcite-disordered dolomite solid-solution series. American Mineralogist,
924   95(11-12), 1650-1656.

925   Zhang, Y.-F., Yao, Q.-Z., Qian, F.-J., Li, H., Zhou, G.-T., and Fu, S.-Q. (2021) Formation pathway of
926   norsethite dominated by solution chemistry under ambient conditions. American
927   Mineralogist, 106(8), 1306-1318.

928   Zhu, C., Donald Rimstidt, J., Zhang, Y., Kang, J., Schott, J., and Yuan, H. (2020) Decoupling feldspar
929   dissolution and precipitation rates at near-equilibrium with Si isotope tracers: Implications for
930   modeling silicate weathering. Geochimica et Cosmochimica Acta, 271, 132-153.
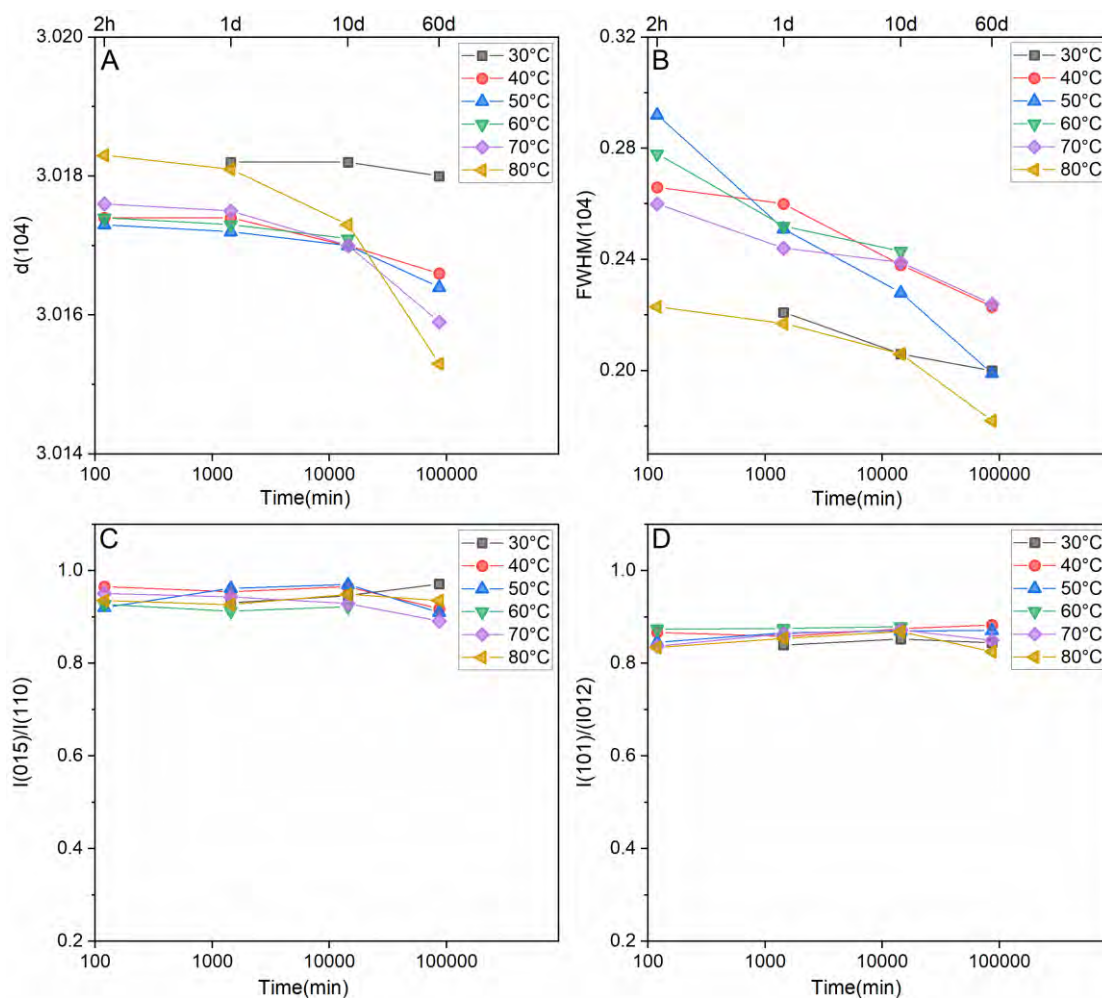
931

932
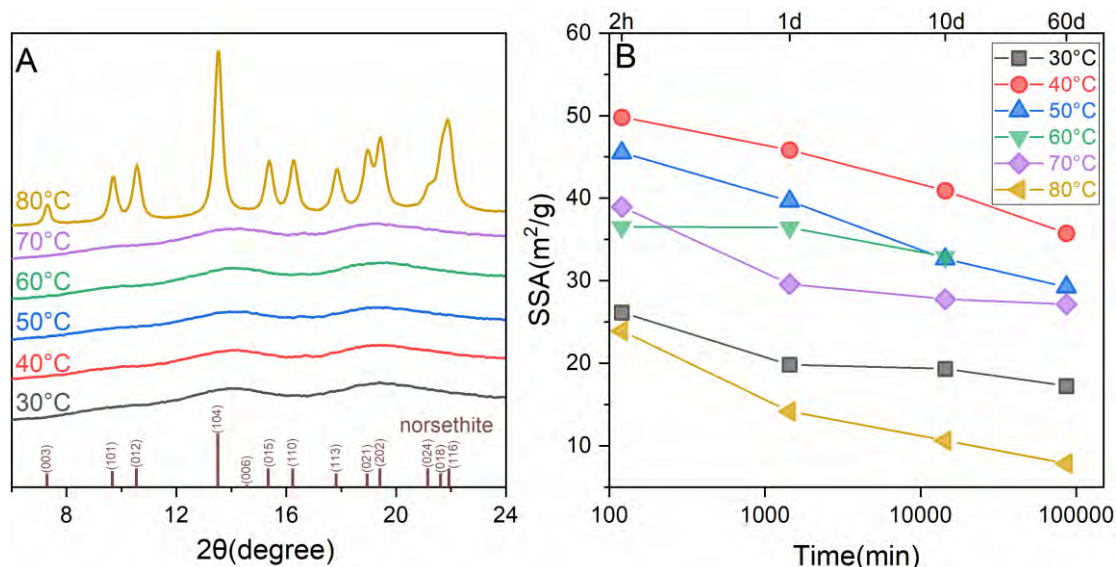
933

934 **FIGURE 1.** (A)XRD patterns of solid products after 1 minute of reaction for
935 experiment set I, (B) Specific Surface Area (SSA) value of solid products versus
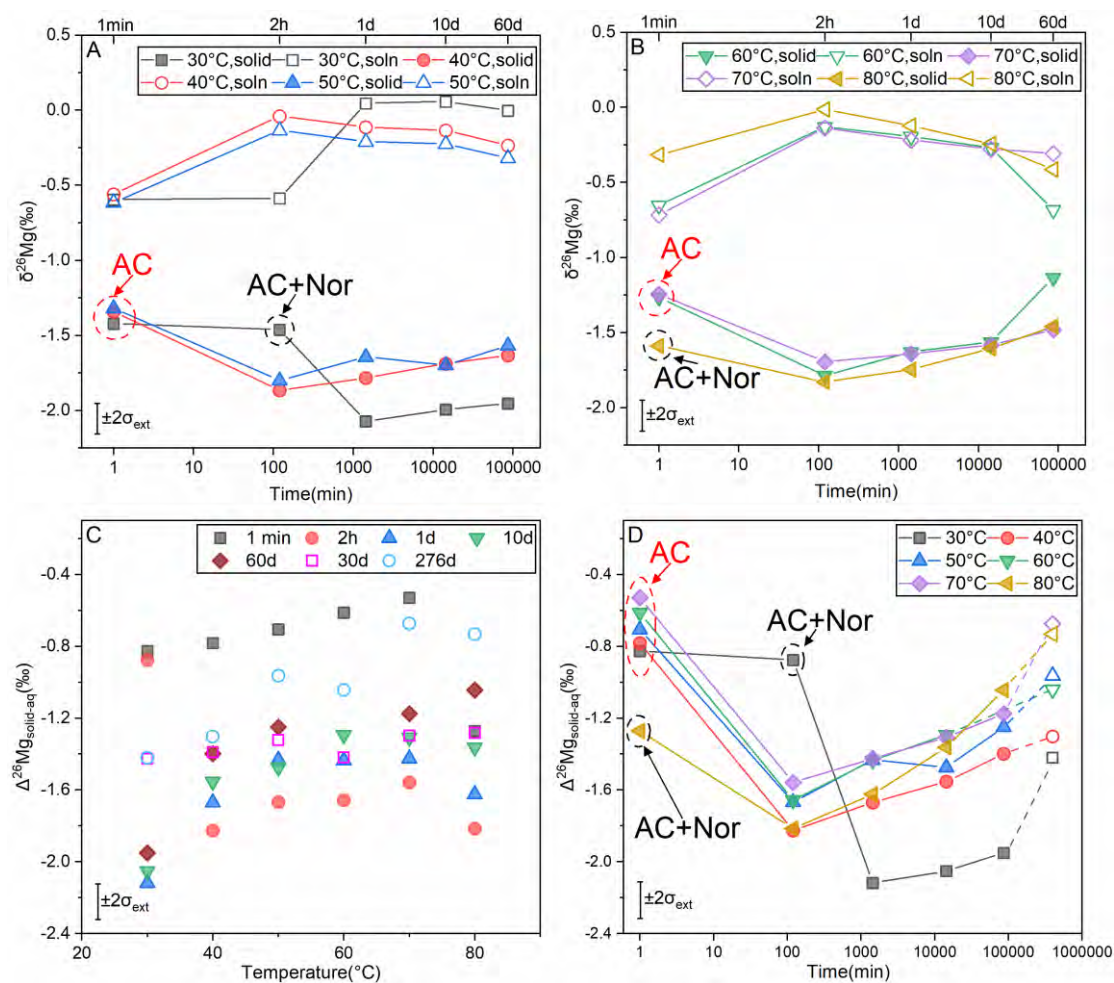936 reaction time.
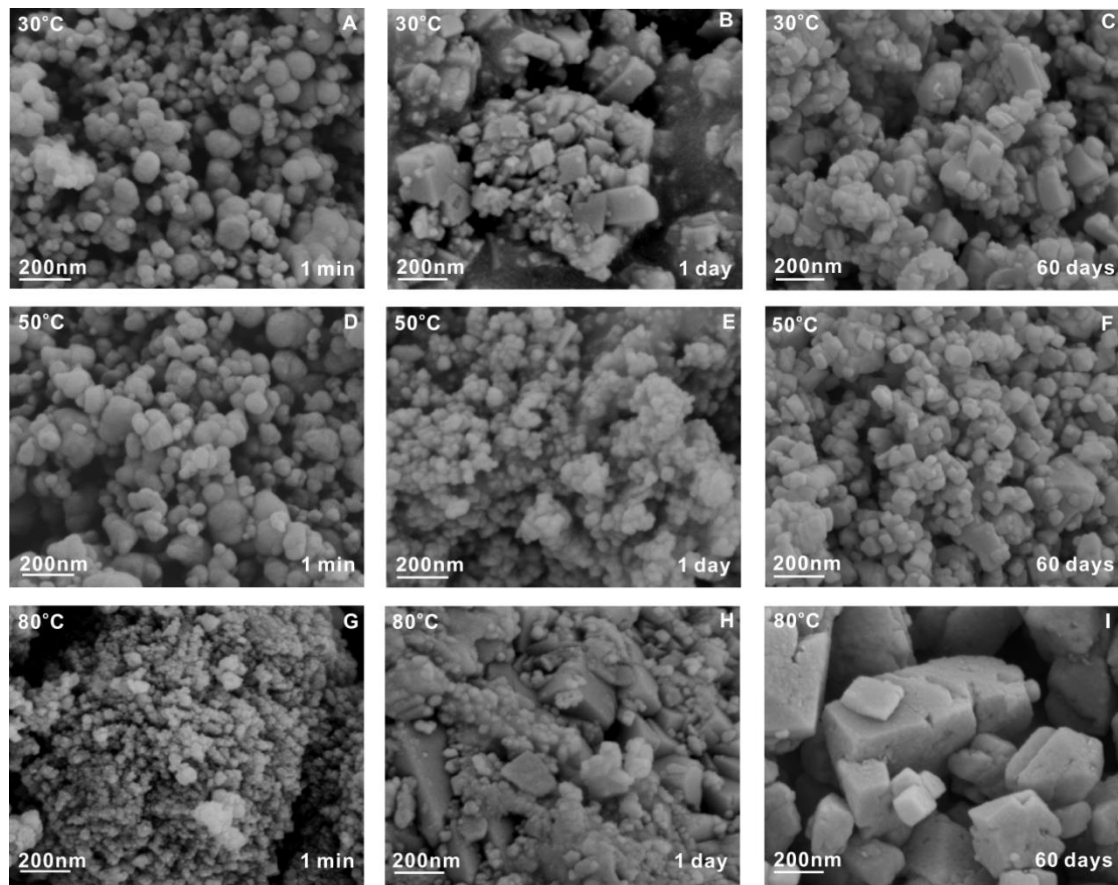
**FIGURE 2.** SEM images of the solid products for experiments Set I. For more details of the experimental conditions, see TableS2.

FIGURE 3. Lattice parameters for norsethite in the synthesis experiments set I. (A) norsethite d(104) versus reaction time, (B) FWHM of (104) peak for norsethite versus reaction time, (C) I(101)/I(012) versus reaction time, (D) I(015)/I(110) versus reaction time.

**FIGURE 4.** (A) δ^{26}Mg values of solid and aqueous phases versus reaction time for experiments at 30 to 50°C. (B) δ^{26}Mg values of solid and aqueous phases versus reaction time for experiments at 60 to 80°C. (C) Δ^{26}Mg$_{solid-aq}$ versus reaction temperature at different reaction time. (D) Δ^{26}Mg$_{solid-aq}$ versus reaction time at different temperature. The solid dots represent the data for experiments Set I, while the hollow dots represent the data for experiments Set II in (C) and (D). AC:amorphous carbonate, Nor:norsethite.
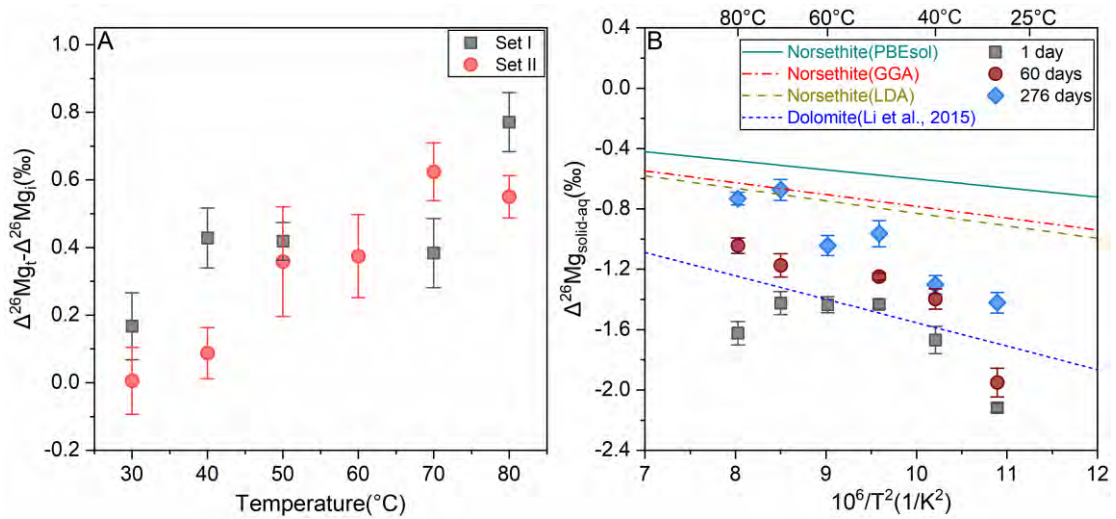
FIGURE 5. (A)The increase in measured $\Delta^{26}Mg_{solid-aq}$ fractionation factors versus temperature, including data from experiment Set I (1 day to 60 days), and data from experiment Set II (30 days to 276 days). Error bar denotes 2 standard deviations. (B) Comparison of experimentally measured (points with error bars) and theoretically calculated (lines) $\Delta^{26}Mg$ factors for norsethite. The temperature-dependent Mg isotope fractionation factor for dolomite suggested by Li et al. (2015) is also plotted for reference.

41

960
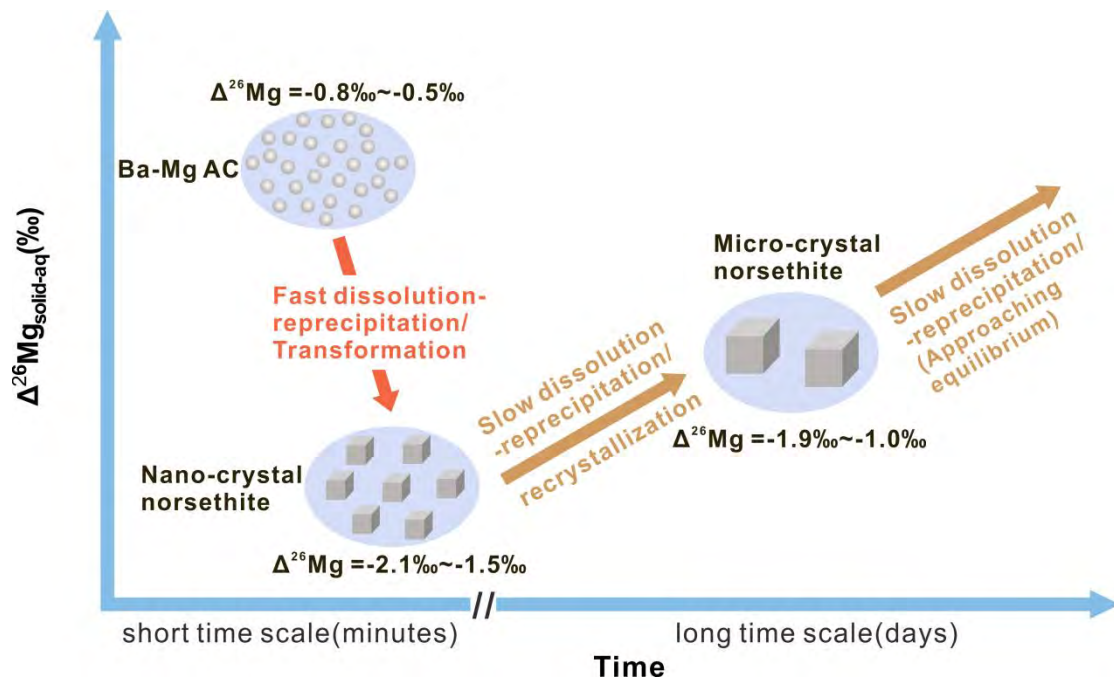
FIGURE 6. A schematic model showing the formation pathway of norsethite and the Mg isotopic fractionation behavior.

963